JMEPEG
https://doi.org/10.1007/s11665-023-08733-4

1059-9495/$19.00

ORIGINAL RESEARCH ARTICLE

Determination of Parameters for Johnson-Cook Dynamic Constitutive and Damage Models for E250 Structural Steel and Experimental Validations

K. Gopinath, V. Narayanamurthy, S.N. Khaderi, and Y.V.D. Rao

Submitted: 13 May 2023 / Revised: 28 July 2023 / Accepted: 4 September 2023

Structural steel (E250 grade) is used in several engineering applications involving loadings from quasi-static to high strain rates (blast discs, explosion vents, etc.), which introduce large deformation, strain and strain rate hardening, thermal softening, and damage to the material. The material's dynamic constitutive behaviour can be aptly modelled by a visco-plasticity-based Johnson–Cook (J–C) strength model and damage initiation and complete failure by the J–C's damage model. In the latter, damage initiation is modelled through continuum damage mechanics and propagation by the fracture mechanics. This paper focuses on the determination of 10 different J–C's dynamic constitutive and damage model parameters for E250 structural steel by conducting several experiments involving tensile tests at different strain rates (0.0003–1.0 s^{-1}), stress triaxialities (0.33–0.95), temperatures (30–800 °C), and SHPB experiments (at 3000 and 8000 s^{-1}). It explains the processes and step-by-step procedures for extracting the model parameters from the experimental results. A different approach is followed in arriving at fracture strain for extracting damage model parameters to suit fracture mechanic-based damage evolution available in the existing FEA codes. The constitutive and damage model parameters thus determined are validated through numerical simulations and comparison with three independent experiments viz. i) experiment of a plain tensile specimen, ii) tensile experiment of a notched specimen, and iii) hydrostatic burst experiment of a flat burst disc. The responses and failure patterns from numerical simulations agreed very well in all three experiments, thereby validating the determined model parameters. The determined model parameters can be utilised directly in the commercially available nonlinear explicit FEA codes.

Keywords E250 structural steel, experimental validation, Johnson–Cook, strain rate, strength and damage models, stress triaxiality

1. Introduction

Structural steel with E250 grade is a work-horse material used in several engineering applications due to its low cost and manufacturability through several methods. Typically, it is used as blast discs, explosion vents, structural construction, etc. These structures and components are subjected to different loadings, from quasi-static to high strain rates, caused by different sources of events such as impact, blast, explosion. Material behaviour under extreme dynamic events differs greatly from static loading conditions. The material undergoes large deformation, strain hardening, strain rate hardening, and

K. Gopinath, Systems Integration (Mechanical), Research Centre Imarat, Hyderabad 500069, India; and Mechanical Engineering, BITS Pilani-Hyderabad, Hyderabad 500078, India; **V. Narayanamurthy**, Systems Integration (Mechanical), Research Centre Imarat, Hyderabad 500069, India; **S.N. Khaderi**, Mechanical and Aerospace Engineering, Indian Institute of Technology Hyderabad, Sangareddy 502285, India; and and **Y.V.D. Rao**, Mechanical Engineering, BITS Pilani-Hyderabad, Hyderabad 500078, India. Contact e-mails: v.nmurthy@gov.in and vbnarayanamurthy@gmail.com.

Abbreviations

A	J–C parameter representing yield stress (MPa)
A_s	Cross-sectional area of SHPB specimen (mm^2)
A_t	Cross-sectional area of the incident and transmitter bars (mm^2)
A_0	Initial cross-sectional area of the tensile specimen (mm^2)
A_f	Cross-sectional area of the tensile specimen after the experiment (mm^2)
B	Strain hardening coefficient (MPa)
C	Strain rate coefficient
c_0	Fundamental longitudinal velocity of the elastic stress wave (m/s)
D_i	Damage initiation variable
D	Damage propagation variable
D_1, D_2, D_3	Stress triaxiality dependent fracture strain parameters
D_4	Strain rate dependent fracture strain parameter
D_5	Temperature dependent fracture strain parameter
E	Young's modulus (MPa)
G_f	Fracture energy (N/mm)
L_s	The thickness of the specimen in the SHPB experiment (mm)
m	Thermal softening exponent
n	Strain hardening exponent
P	Equivalent force in the incident and transmitted bar (N)

Published online: 10 November 2023

P_1, P_2	Forces on the left and right end of the specimen in SHPB experiment (N)
$\dot{P}$	Incident pressure loading rate in burst experiment (MPa/s)
P_b	Burst pressure (MPa)
T	Temperature in material (°C)
T^*	Homologous temperature (°C)
T_0	Reference temperature (°C)
T_m	Melting temperature of the material (°C)
t	Time interval for the stress wave propagation through an element (s)
t_d	Natural time period (s)
u_1, u_2	Displacements at the left and right end of the specimen in the SHPB experiment
u^{pl}	Plastic displacement
u_f^{pl}	Plastic displacement at failure
w_l	Crack tip opening displacement (mm)
x, y	Horizontal and vertical coordinate axes, respectively
σ	True stress/von-Mises tensile flow stress (MPa)
σ_m	Average of the three normal stresses, i.e. mean stress (MPa)
$\tilde{\sigma}$	Von-Mises equivalent stress (MPa)
σ^*	Dimensionless pressure, i.e. stress ratio or stress triaxiality
σ_0	Stress at the onset of damage (MPa)
σ_t	Tensile strength of the material (MPa)
σ_y	Dynamic yield stress (MPa)
σ_D	Stress at damaged state (MPa)
ε	True strain/plastic strain
ε_0	Equivalent plastic strain at the onset of damage
$\dot{\varepsilon}$	Strain rate (s^{-1})
$\dot{\varepsilon}_0$	Reference strain rate (s^{-1})
$\dot{\varepsilon}^*$	Dimensionless normalised plastic strain rate
$\dot{\varepsilon}_s$	Strain rate in SHPB specimen (s^{-1})
ε_f	Fracture strain
ε_i	Incident strain pulse
ε_r	Reflected strain pulse
ε_s	Strain in SHPB specimen
ε_t	Transmitted strain pulse
$\Delta\varepsilon$	Incremental plastic strain
ω_n	Fundamental natural frequency (Hz)
ρ	Density of the material (kg/m^3)

thermal softening, eventually leading to damage initiation, propagation, and failure.

The behaviour of this material under such extreme loadings can be numerically simulated using nonlinear explicit finite element analyses (FEA) based on Lagrangian, Eulerian, arbitrary Lagrangian–Eulerian, or meshless methods along with appropriate models to capture the material's constitutive (i.e. strength) and damage behaviour. Of several material and damage models available in the literature, the strength and damage models of Johnson–Cook (J–C) are quite popular (Ref 1-3). Although J–C models are one of the oldest models, they are increasingly finding their applications in impact simulations due to their several advantages. The primary advantage is that the material behaviours or effects can be isolated independently, and appropriate material and damage model parameters can be determined from simple experiments. However, the number of experiments and their conditions depend on the level of accuracy of the experimental results. Researchers have attempted to determine either few or all (A, B, n, C, and m) material parameters of the J–C strength model and ($D_1 \ldots D_5$) damage parameters of the J–C damage model for different engineering materials through various experimental techniques such as uniaxial tensile experiments, Split Hopkinson Pressure Bar (SHPB) experiments conducted at different strain rates and temperatures. Vedantam et al. (Ref 4) attempted for Mild steel and DP590 steel; Xu et al. (Ref 5) for 603 Armour steel; Banerjee et al. (Ref 6) for Armour steel; Farahani et al. (Ref 7) for Inconel-718; Murugesan et al. (Ref 8) for AISI-1045; Majzoobi et al. (Ref 9) for an unspecified engineering material; and Bal et al. (Ref 10) for Aluminium alloy 7068-T651. Few have obtained these parameters through several numerical iterations, starting with approximate values until their intended responses match with benchmark experiments.

Vedantam et al. (Ref 4) obtained the J–C strength model constants (except temperature dependent parameter, m) of mild steel and DP590 steel using uniaxial tensile experiments at a strain rate of 0.001 s^{-1} and SHPB experiments at strain rates of 267, 800, and 1800 s^{-1} and concluded that mild steel having lower yield strength exhibited higher strain rate sensitivity than DP590 steel having higher yield strength. Xu et al. (Ref 5) investigated the plastic behaviour of 603 Armour steel (a low-alloy medium carbon steel heat treated to produce a tempered martensitic microstructure) through quasi-static uniaxial compression experiments at strain rates ranging from 0.001 to 0.1 s^{-1} and dynamic compression experiments using SHPB at strain rates 200, 2000 and 4500 s^{-1} at temperatures ranging from 15 to 600 °C. The evaluated J–C strength model parameters are assessed by comparing the predicted results with strain rate jump test experiments of a separate specimen and shown that the error in prediction of flow stress by the J–C model is 16.6% in quasi-static condition and 13% in dynamic condition for this steel. Banerjee et al. (Ref 6) attempted to determine all the J–C strength and damage model parameters of the Armour steel through uniaxial tension experiments at various strain rates between 0.0001 and 150 s^{-1} and temperatures ranging from room temperature to 500 °C and validated their determined J–C model parameters by comparing numerical simulations with Charpy impact test.

Farahani et al. (Ref 7) determined the J–C plasticity model parameters of Inconel-718 except for strain rate dependent parameters using quasi-static uniaxial tension experiments at a strain rate of 0.1 s^{-1} and temperatures of 400, 475, 550, and 625 °C. Since the strain rate dependent parameter was required at a strain rate more than 10^6 s^{-1} for their intended application, they determined this parameter iteratively through the trail-and-error method by comparing the crater produced by the indentation of steel ball in an impact experiment with the numerical simulation. Murugesan et al. (Ref 8) extracted the J–C strength and damage model parameters of AISI-1045 medium carbon steel by several isothermal hot uniaxial tensile experiments at strain rates varying from 0.05 to 0.1 s^{-1} and at temperatures ranging from 650 to 950 °C and proposed a nonlinear algorithm to optimise the extracted parameters and minimise the error between the predicted and experimental flow stress.

Majzoobi et al. (Ref 9) determined the J–C's material and damage model constants (except temperature dependent parameters) of an unspecified engineering material. They performed limited experiments and determined the strain rate-independent material model parameters from the quasi-static experiment of a regular specimen and strain rate-independent damage parameters through numerical iterations. They finalised the model

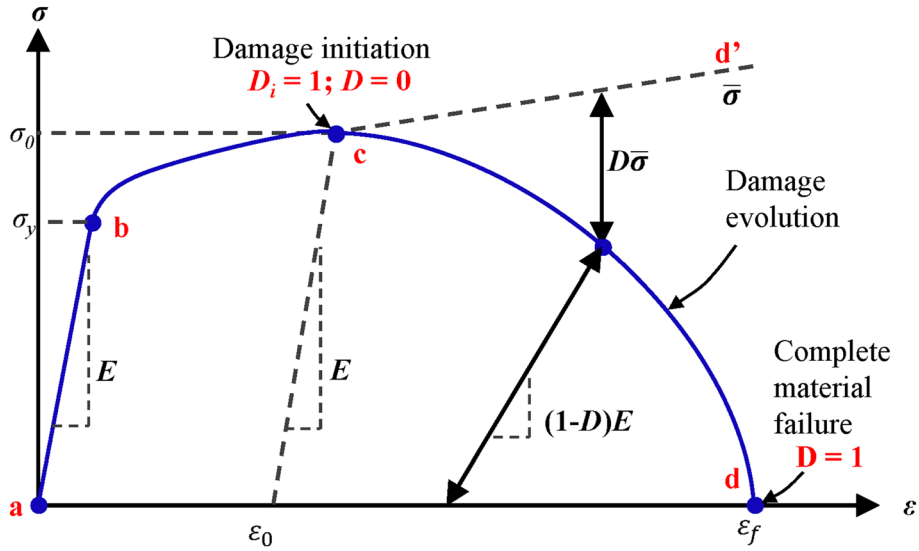

Fig. 1 Implementation of damage evolution

parameters by matching the experimental damage profile with FEA simulations of a notched specimen using an optimisation technique. They also adopted a similar optimisation approach for determining the strain rate dependent strength and damage parameters of J–C models from the experimental results of flying wedge high-rate testing device and validated the extracted model parameters through FEA simulations of fractured specimens and comparison with experiments. Bal et al. (Ref 10) determined the J–C material parameters of Aluminium alloy 7068-T651 by conducting experiments using uniaxial experiments at quasi-static strain rate, Gleeble tests at temperatures up to 300 °C and strain rates up to 100 s^{-1} and SHPB experiments at higher strain rates and proposed three different sets of values for J–C material model parameters for different applications with maximum, average, and minimum plastic strains.

Although E250 structural steel is used in several engineering applications which involve different loadings ranging from quasi-static to high strain rates, the J–C strength and damage model parameters needed for its numerical simulation are not available in the literature. This paper is intended to present the processes and procedures involved in determining 10 different strength and damage model parameters of the J–C model for E250 structural steel through several experiments involving tensile tests at different temperatures (30-800 °C), strain rates (0.0003-1.0 s^{-1}) and stress triaxialities (0.33-0.95), and SHPB experiments (at 3000 and 8000 s^{-1}). A different approach is proposed here to determine the critical fracture strain and J–C damage parameters which facilitates the adoption of the determined damage parameters in any commercial available nonlinear explicit FEA code. The determined model parameters are validated by numerically simulating i) a tensile experiment of a plain specimen, ii) a separate tensile experiment of a notched specimen, and iii) a hydrostatic experiment of a burst disc.

2. Johnson–Cook Dynamic Strength and Failure Models and Implementation of Damage Evolution

The material's constitutive behaviour is modelled with the Johnson–Cook strength model and its failure through the Johnson–Cook damage model. These two models define the material's visco-plasticity and damage behaviour during loading in numerical simulation.

2.1 Johnson–Cook Strength Model

The dynamic flow stress–plastic strain relationship for metallic materials undergoing plastic deformation is best described by Johnson–Cook constitutive relation (Ref 1, 2) which is given as follows:

$$\sigma = [A + B\varepsilon^n][1 + C\ln\dot{\varepsilon}^*][1 - T^{*m}] \quad \text{(Eq 1)}$$

where σ is the von-Mises flow stress, ε is the equivalent plastic strain, $\dot{\varepsilon}^* = \dot{\varepsilon}/\dot{\varepsilon}_0$ is the dimensionless normalised plastic strain rate considering the reference strain rate $\dot{\varepsilon}_0$, $\dot{\varepsilon}$ is the strain rate, and $T^* = (T - T_0)/(T_m - T_0)$ is the homologous temperature of the material. A is the yield strength of the material, B is the strain hardening coefficient, n is the strain hardening exponent, C is the strain rate coefficient, m is the thermal softening parameter, T_0 is the reference temperature, and T_m is the melting temperature of the material. The first, second, and third terms in Eq 1, respectively, capture the large strain, strain rate, and thermal softening effects during loading.

2.2 Johnson–Cook Damage Model

The Johnson–Cook damage model is based on the fracture strain of the metallic material and depends on stress triaxiality, strain rate and temperature (Ref 1, 3). The initiation of damage in the material element is defined by:

$$D_i = \sum \frac{\Delta\varepsilon}{\varepsilon_f} \quad \text{(Eq 2)}$$

where $\Delta\varepsilon$ is the incremental plastic strain during the integration cycle, and ε_f is the fracture strain which is given by:

$$\varepsilon_f = [D_1 + D_2 \exp(D_3\sigma^*)][1 + D_4 \ln \dot{\varepsilon}^*][1 + D_5 T^*] \quad \text{(Eq 3)}$$

where $\sigma^* = \sigma_m/\tilde{\sigma}$ is the dimensionless pressure, i.e. stress ratio, σ_m is the mean stress, $\tilde{\sigma}$ is the von-Mises equivalent stress, and $D_1 \dot{s}.D_5$ are the damage constants for the material, which are determined from experiments. This model assumes that the fracture suddenly occurs when $D_i = 1$. However, the material strength degrades after a certain critical strain due to the development of internal cracks, which is further explained in the next section.

2.3 Implementation of Damage Evolution

A typical stress–strain response of metals under uniaxial loading conditions is shown in Fig. 1. Curve a-b represents the linear elastic phase, curve *b-c* represents the strain hardening phase, and point *c* represents the onset of damage beyond which the load carrying capacity of the material decreases due to the development of macro cracks. Curve *c-d* represents material behaviour with damage evolution. Without damage evolution, stress–strain response follows the curve *c-d'*. At point c, σ_0 and ε_0 are, respectively, the stress and equivalent plastic strain at the onset of damage where $D = 0$ and, ε_f is the equivalent plastic strain at failure where damage variable $D = 1$.

In the damage evolution phase, material strength reduces due to the degradation of the elastic stiffness of the material and stress at any point of loading is governed by the scalar damage equation given as follows:

$$\sigma_D = (1 - D)\overline{\sigma} \quad \text{(Eq 4)}$$

where σ_D is stress at the damaged state, D is the damage propagation variable, and $\tilde{\sigma}$ is the undamaged stress which is the stress obtained from the Johnson–Cook constitutive relation given in Eq 1.

The damage model proposed by Johnson–Cook assumes that damage accumulates in the material element during plastic straining and that the material fails immediately when damage reaches a critical value. But the material strength degrades with damage, and experiments indicate that the effect of damage on the material strength remains zero during the build-up of dislocations generating micro cracks (Ref 11). Based on these observations, a unified model for damage (Ref 11) is given by:

$$\sigma_D = (1 - D)[A + B\varepsilon^n][1 + C \ln \dot{\varepsilon}^*][1 - T^{*m}] \quad \text{(Eq 5)}$$

where $D = 0$ for undamaged material and $D = 1$ for fully fractured material. There exists a threshold of accumulated plastic strain at which the damage starts to evolve (Ref 11, 12). In the present work, damage initiation is assumed to be starting when the accumulated plastic strain reaches a critical value. Then, the stress–strain relation follows Eq 5 after fracture initiation. The present work follows fracture mechanics-based damage evolution, which is explained in detail in sect. 4.3.

Table 1 Chemical composition of E250 structural steel (% mass)

C	Mn	Si	P	S	Fe
0.2–0.23	1.5	0.4	0.045, max	0.045, max	Remainder

3. Experiments for Material Characterisation

E250 Structural steel is a medium carbon steel with a minimum yield strength of 250 MPa, and its chemical composition obtained from a spectroscopic analysis is given in Table 1. The specimens are made from 2 mm thick hot rolled sheets by laser cutting. Two batches of specimens are experimented, and their results are averaged. In total, 16 types of experiments were conducted, and their list is given in Table 2. All tensile experiments at room temperature are

Table 2 Details of experiments and specimens for determining parameters of Johnson–Cook material and damage models

J–C parameter		Experiment	Specimen no.	Temperature, °C	Stress triaxiality, σ^*	Strain rate, s^{-1}
A, B, n		Tensile	1 (a, b)	30	0.33	3×10^{-4}
C	D_4		1 (a, b)	30	0.33	3×10^{-4}
			2 (a, b)		0.33	3×10^{-3}
		Tensile	3 (a, b)		0.33	3×10^{-2}
			4 (a, b)		0.33	3×10^{-1}
			5 (a, b)		0.33	4×10^{-1}
			6 (a, b)		0.33	1×10^{0}
		SHPB	7 (a, b)	30	…	3×10^{3}
			8 (a, b)		…	8×10^{3}
D_1, D_2, D_3		Tensile (notched specimens at various σ^*)	9 (a, b)	30	0.33	3×10^{-4}
			10 (a, b)		0.49	3×10^{-4}
			11 (a, b)		0.70	3×10^{-4}
			12 (a, b)		0.95	3×10^{-4}
m, D_5		Tensile	13 (a, b)	200	0.33	3×10^{-4}
			14 (a, b)	400	0.33	3×10^{-4}
			15 (a, b)	600	0.33	3×10^{-4}
			16 (a, b)	800	0.33	3×10^{-4}

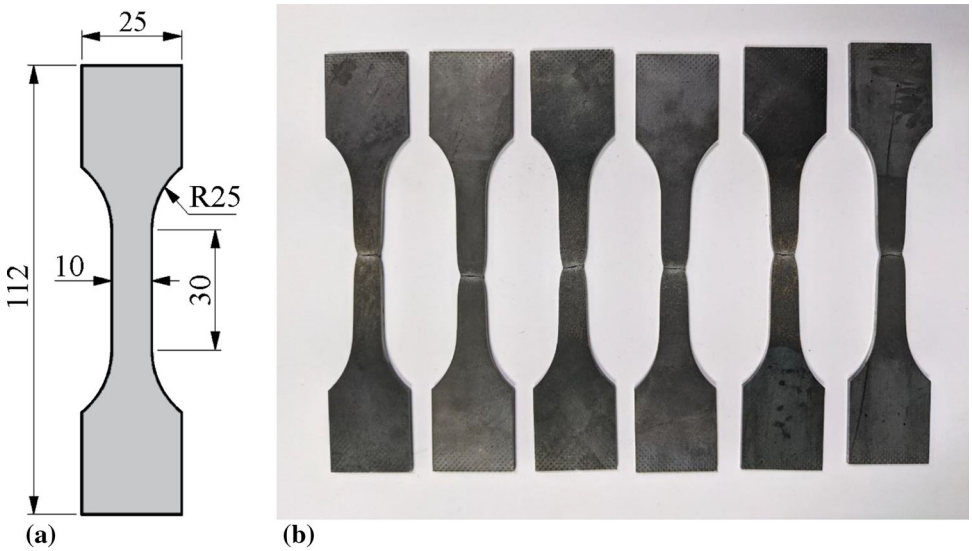

Fig. 2 Plain specimens for uniaxial tensile experiments at various strain rates at room temperature. (a) Specimen geometry (thickness = 2.0 mm) (all dimensions in mm). (b) Experimented specimens 1–6 (Batch-a)

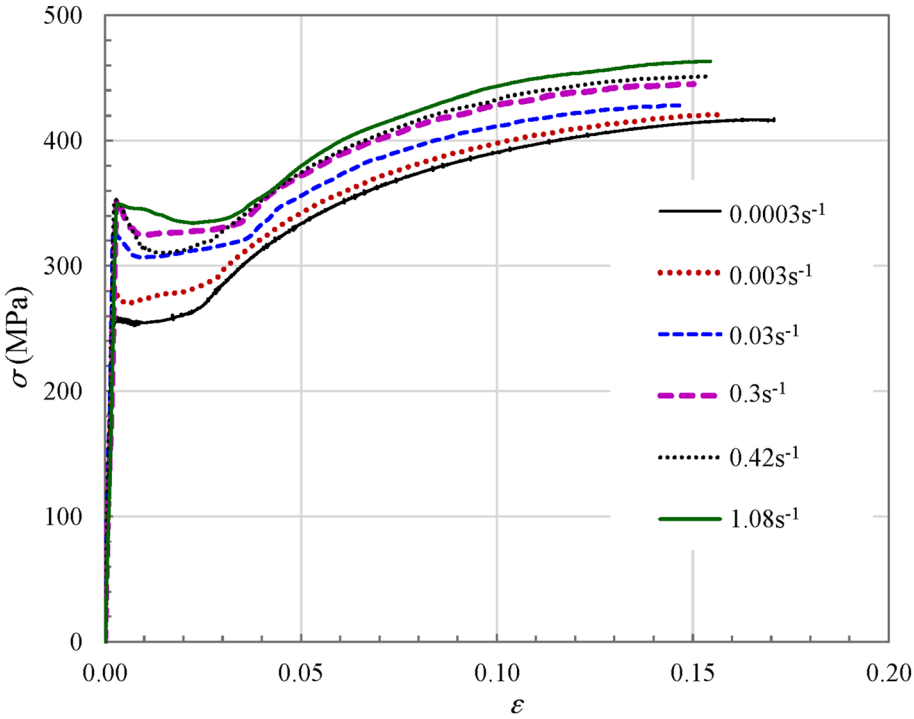

Fig. 3 Averaged true stress–true strain curves of plain tensile specimens at various strain rates obtained from tensile experiments at room temperature

conducted on BiSS make servo-hydraulic controlled universal testing machine (UTM) with a maximum capacity of 25 kN. High temperature tensile experiments are conducted on INSTRON make electro-mechanically controlled UTM with an attached furnace having a maximum capacity of 600 kN. SHPB experiments are conducted on circular specimens to obtain stress–strain curves at higher strain rates. All experiments are broadly classified into four categories, viz. 1) tensile experiments at different strain rates, 2) SHPB experiments at higher strain rates, 3) tensile experiments of notched specimens, and 4) tensile experiments at different temperatures to obtain the Johnson–Cook model parameters, as shown in Table 2.

In the SHPB setup, all bars are made of D2 tool steel with a hardness of more than 50 HRC and a diameter of 12 mm. The incident bar and transmission bars have a length of 1200 mm. For low and high strain rate experiments, striker length is 300

and 200 mm, respectively. The strain pulses were recorded using foil strain gauges of gauge length 2 mm through a high-speed amplifier and National Instruments data acquisition system.

3.1 Tensile Experiments at Various Strain Rates

Six types of tensile experiments were conducted on 12 specimens at room temperature at strain rates of 0.0003, 0.003, 0.03, 0.3, 0.4, and 1.0 s^{-1}. Specimen geometry used in these experiments is shown in Fig. 2(a), and the first batch of specimens after experiments are shown in Fig. 2(b). The average true stress–true strain curves obtained from experiments are shown in Fig. 3. The material has exhibited strain rate sensitivity, as seen in the stress–strain curves where its yield and ultimate tensile strengths increased with increased strain rate.

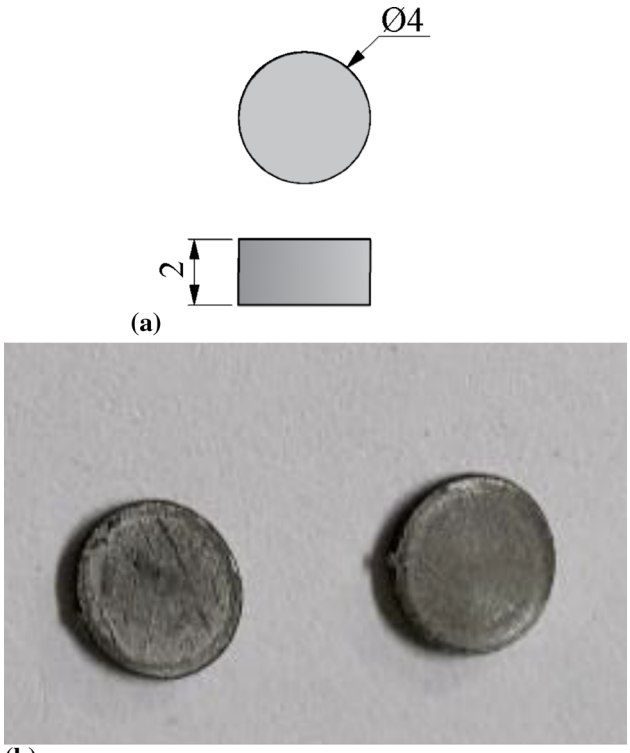

Fig. 4 Specimens for SHPB experiments at higher strain rates. (a) Specimen geometry (all dimensions in mm). (b) Experimented specimens 7 and 8 (Batch-a)

3.2 SHPB Experiments at Higher Strain Rates

The basic principle governing the SHPB is that the impact stress waves travelling through the specimen (i.e. material to be tested) are fast enough that the time interval for propagation is much smaller than the total time of the experiment. This permits several reflections to occur at the ends of the tested specimen, which reasonably presents a uniform state of stress and strain. This uniaxial stress state is ensured by using a lubricant between the ends of the bars and specimen. Finally, it is assumed that the stresses and velocities in the specimen ends are transmitted through the input and output bars without any dispersion. Simple expressions for stress, strain, and strain rate in the specimen are obtained by assuming and adopting the same material and cross-sectional area for both input and output bars.

Let c_0 be the fundamental longitudinal velocity of the elastic stress wave in the bar, given by:

$$c_0 = \sqrt{\frac{E}{\rho}} \qquad \text{(Eq 6)}$$

in which E and ρ are, respectively, the elastic modulus and density of the material of the bar. The displacements u_1 and u_2 at the left and right ends of the specimen can be written in terms of the incident ε_i, reflected ε_r and transmitted ε_t strain pulses as follows:

$$u_1 = c_0 \int_0^t (\varepsilon_i - \varepsilon_r)\, dt \qquad \text{(Eq 7a)}$$

and

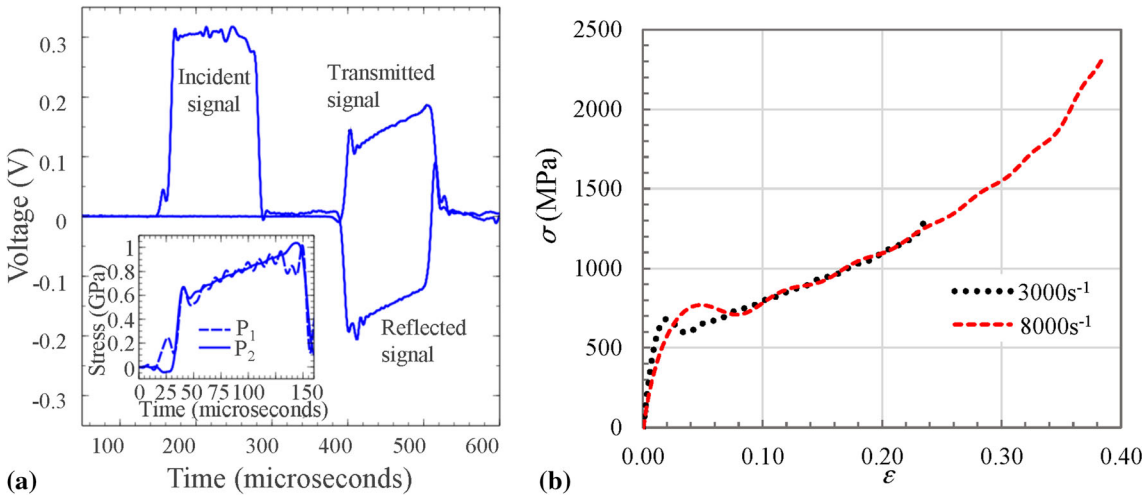

Fig. 5 Typical strain signals from SHPB setup and true stress–true strain curves obtained from SHPB experiments. (a) Typical strain signals obtained from SHPB setup (*Inset:* The force balance of the sample, i.e. the stress acting on the sample-incident bar and sample-transmission bar interfaces represented by P_1 and P_2, respectively). (b) Averaged true stress–true strain curves of specimens 7 and 8 at higher strain rates

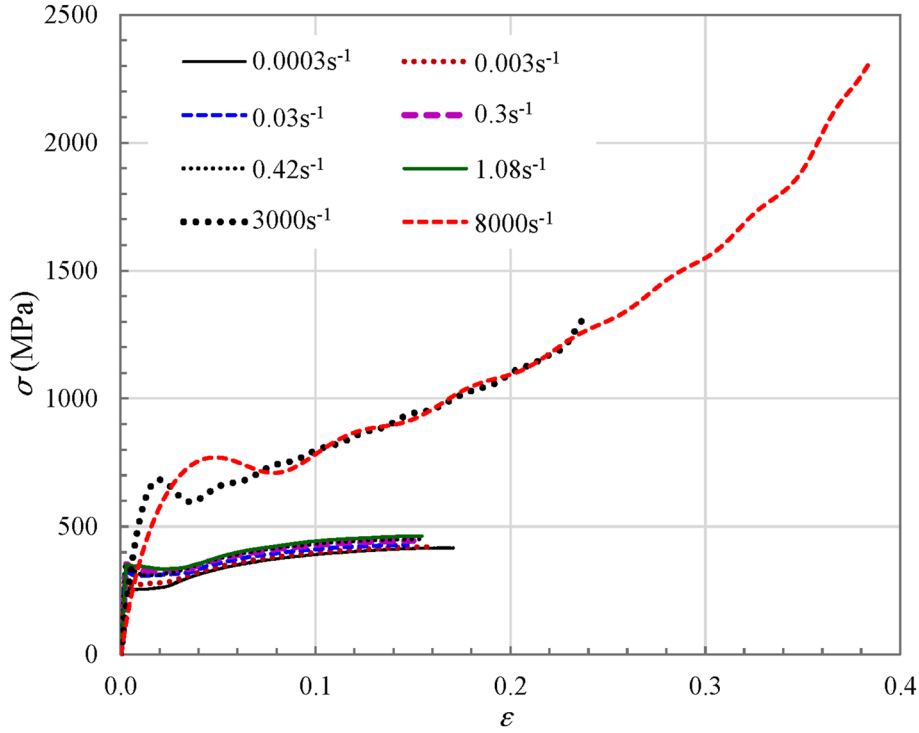

Fig. 6 Averaged true stress–true strain curves of specimens 1–8 at different strain rates

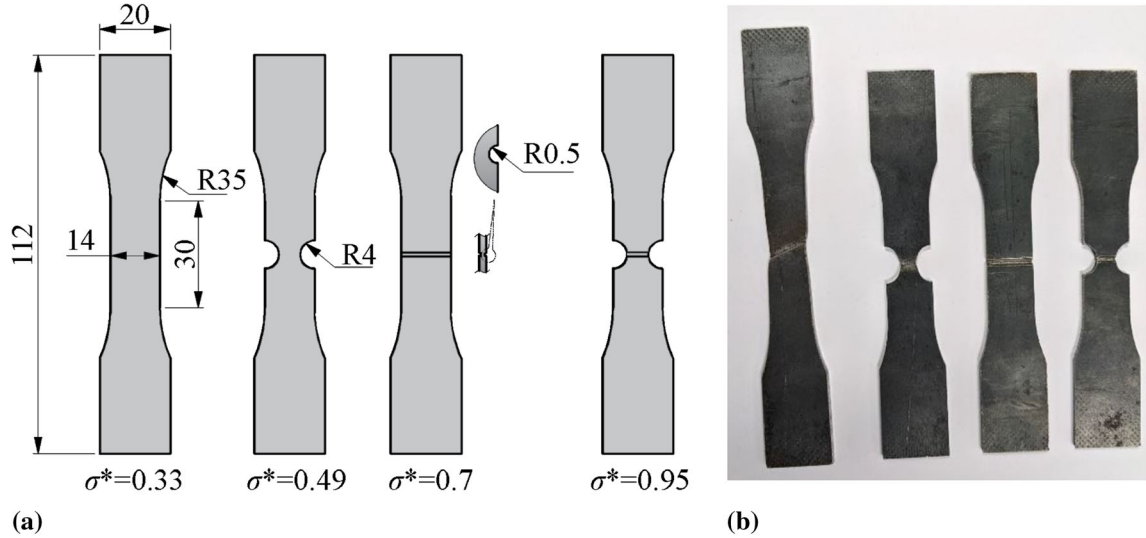

Fig. 7 Notched specimens at different stress triaxiality (σ^*). (a) Specimen geometry (thickness = 2.0 mm) (all dimensions in mm). (b) Specimens 9–12 (Batch-a) after the experiments

$$u_2 = c_0 \int_0^t \varepsilon_t \, dt \qquad \text{(Eq 7b)}$$

where t is the time interval for the stress wave propagation through the specimen. Here, the compressive stresses and strains have a positive sign. Due to the assumption of the uniform state of stress and strain through the length, i.e. thickness of the specimen L_s, the strain in the specimen ε_s is given by:

$$\varepsilon_s = \frac{u_1 - u_2}{L_s} \qquad \text{(Eq 8)}$$

Substituting Eq 7a, b into Eq 8 provides

$$\varepsilon_s = \frac{c_0}{L_s} \int_0^t (\varepsilon_i - \varepsilon_r - \varepsilon_t) \, dt \qquad \text{(Eq 9)}$$

The forces P_1 and P_2 acting, respectively, at the left and right ends of the specimen are given by:

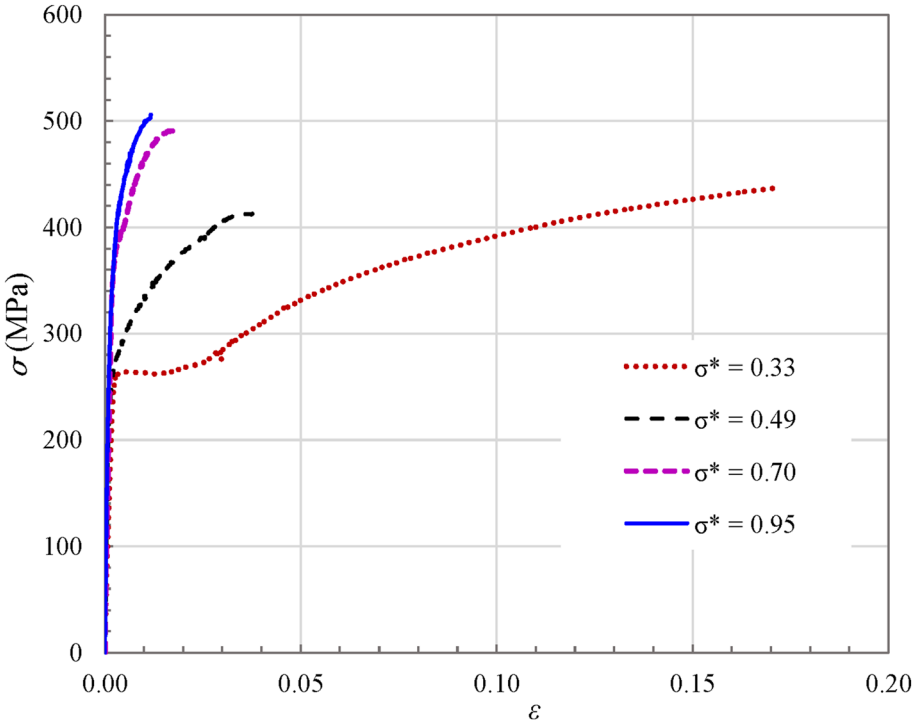

Fig. 8 Averaged true stress–true strain curves of specimens 9–12 at various σ^* (at a strain rate value = 0.0003 s^{-1})

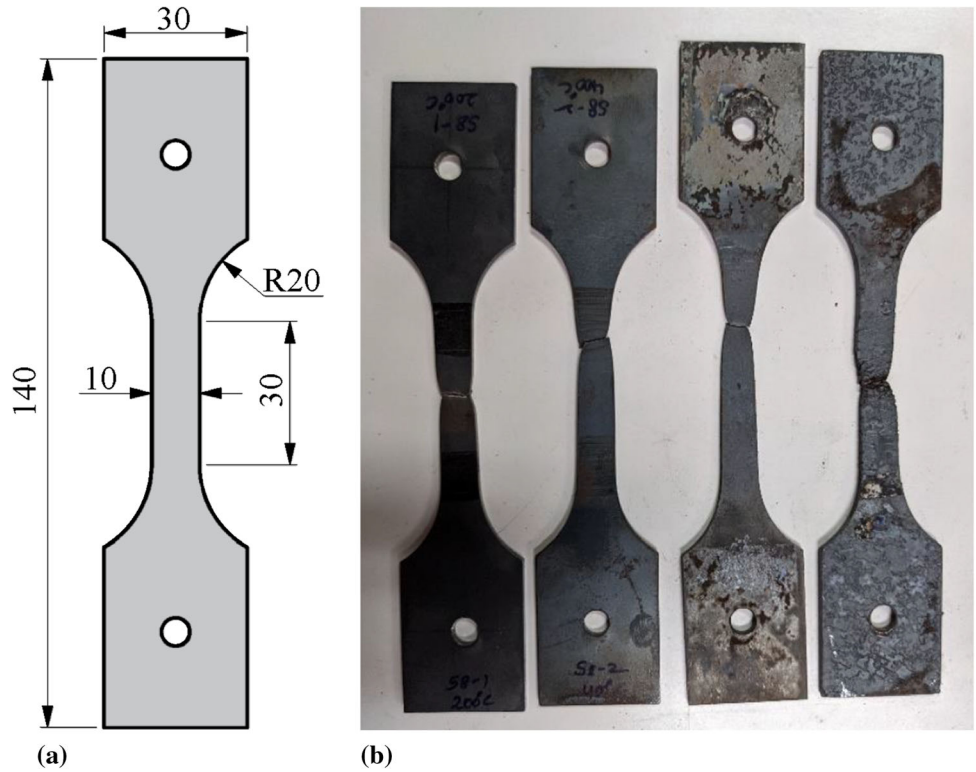

Fig. 9 Specimens for tensile experiments at elevated temperatures (at strain rate = 0.0003 s^{-1}). (a) Specimen geometry (thickness = 2.0 mm) (all dimensions in mm). (b) Specimens 13–16 (Batch-a) after the experiments

$$P_1 = EA_t\,(\varepsilon_i + \varepsilon_r) \quad \text{(Eq 10a)}$$

and

$$P_2 = EA_t\,\varepsilon_t \quad \text{(Eq 10b)}$$

where A_t is the cross-sectional area of the incident and transmitter bars. The specimen is in equilibrium under the action of the above forces, i.e. $P_1 = P_2 = P$. So, Eq 10a, b yields $\varepsilon_t = 0.33\text{em}\varepsilon_i + \varepsilon_r$. Therefore, the stress, strain, and strain rate acting on the specimen can be obtained, respectively, from the following equations:

$$\sigma_s = \frac{P}{A_s} = E\varepsilon_t \frac{A_t}{A_s} \quad \text{(Eq 11a)}$$

$$\varepsilon_s = \frac{-2c_0}{L_s} \int_0^t \varepsilon_r \, dt \quad \text{(Eq 11b)}$$

$$\dot{\varepsilon}_s = \frac{-2c_0}{L_s} \varepsilon_r \quad \text{(Eq 11c)}$$

where A_s is the cross-sectional area of the specimen.

The response of the specimen material under dynamic loads can be characterised by accurately measuring the reflecting and transmitted impact waves and by knowing the elastic modulus, density, and cross-sectional area of the bar and the cross-sectional area and length of the specimen.

SHPB experiments were conducted on four circular specimens at room temperature and strain rates of 3000 and 8000 s^{-1}. Specimen geometry used in these experiments is shown in Fig. 4(a), and the first batch of specimens after experiments are shown in Fig. 4(b). The impact waves are measured with strain gauges, as shown in Fig. 5(a), by acquiring the strain signals from the strain gauge mounted on the bars. The inset of Fig. 5(a) shows the force balance of the sample, i.e. the specimen. Stress acting on the sample-incident bar and sample-transmission bar interfaces is represented by P_1 and P_2, respectively. The sample is in equilibrium. The averaged true stress–true strain curves obtained from SHPB experiments using Eq 11a–c are shown in Fig. 5(b). These stress–strain data demonstrated a phenomenal increase in the strength of the material at higher strain rates. True stress–true strain curves at all strain rates are shown in Fig. 6.

3.3 Tensile Experiments of Notched Specimens

Tensile experiments were conducted on two sets of 4 notched specimens with various stress triaxiality (σ^*) values. The values of stress triaxialities are found to be 0.33, 0.49, 0.7, and 0.95. These values are obtained through the FEA simulation of each notched specimen, and the procedure followed to obtain these values is explained in Sect. 4.2.2. The geometry of these notched specimens is shown in Fig. 7(a), and the first batch of the experimented specimens is shown in Fig. 7(b). Averaged true stress–true strain curves of notched specimens obtained from these experiments are shown in Fig. 8. The experimental results exhibited a substantial decrease in failure strain and a marginal change in ultimate strength when the stress triaxiality is increased from 0.33 to 0.49; and from 0.49 to 0.7; a decrease in failure strain and an increase in

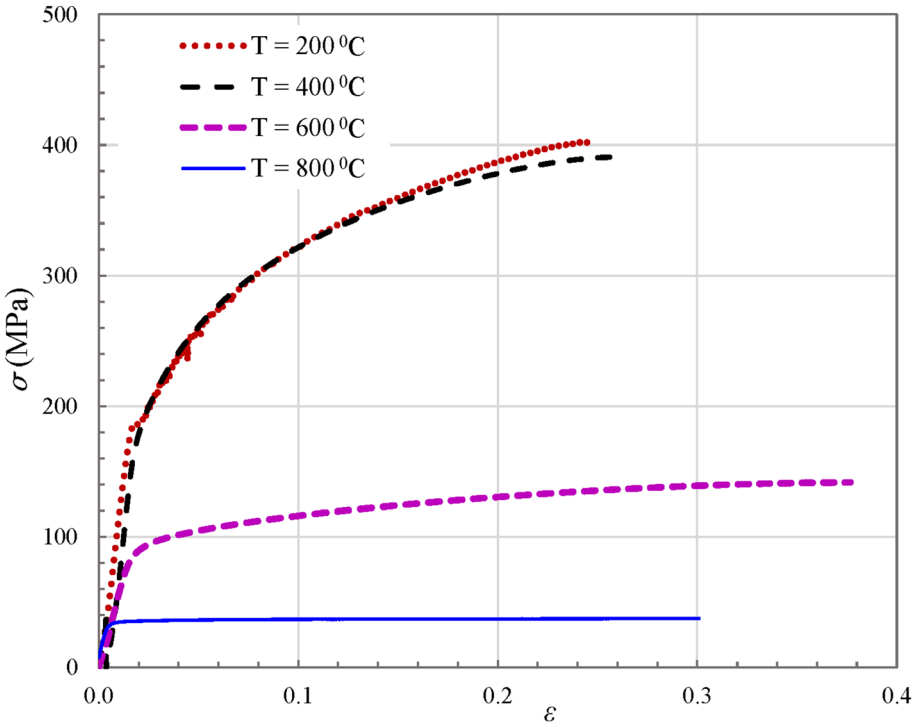

Fig. 10 Averaged true stress–true strain curves of specimens 13–16 at elevated temperatures (at strain rate = 0.0003 s^{-1})

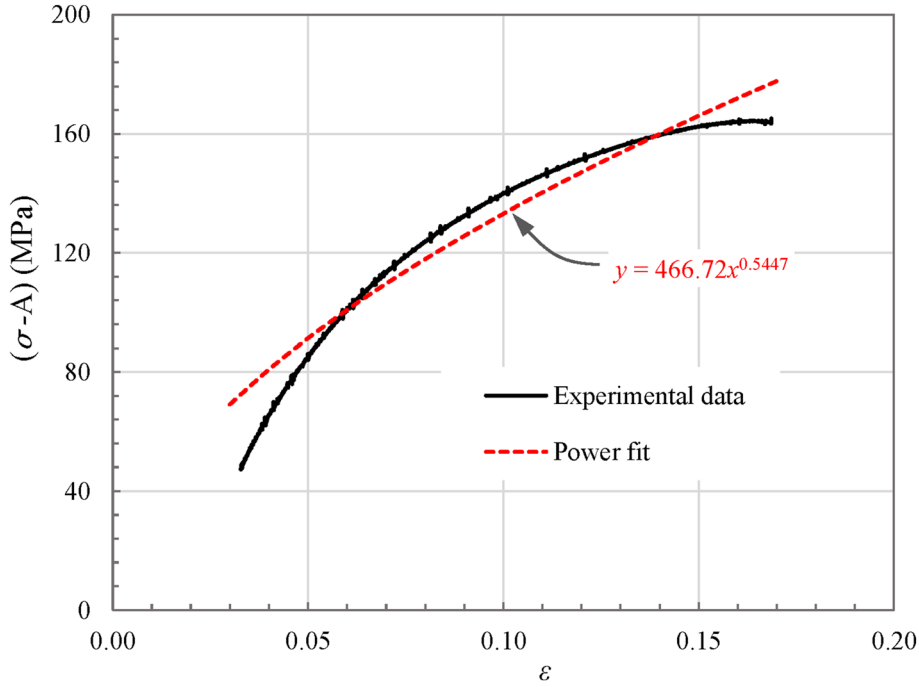

Fig. 11 Determination of B and n

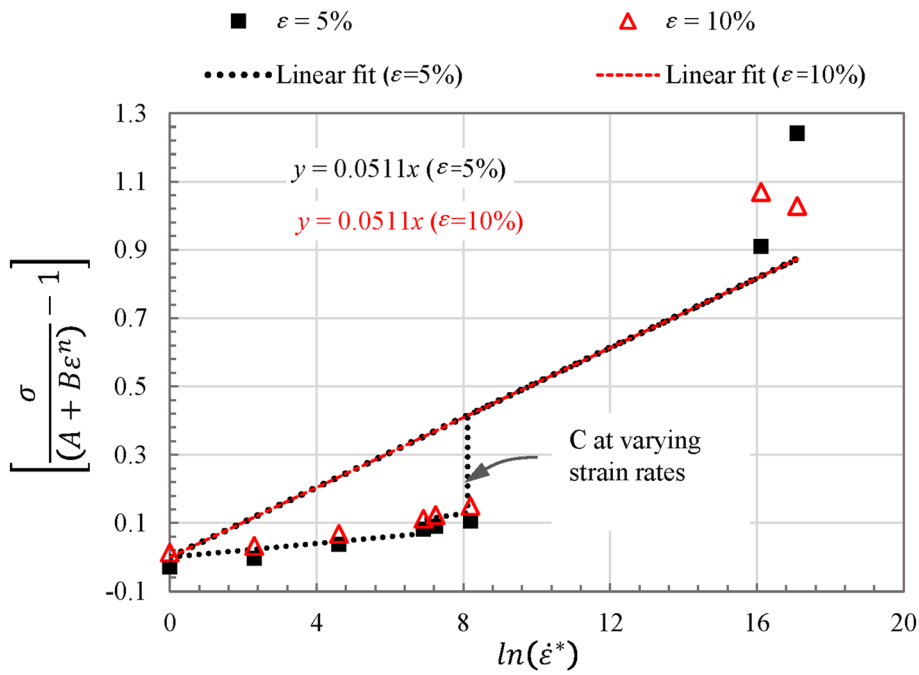

Fig. 12 Determination of C

ultimate strength are observed, but after 0.7, the changes in responses are minimal.

3.4 Tensile Experiments at Elevated Temperatures

Tensile experiments were conducted on two sets of 4 specimens at elevated temperatures of 200, 400, 600, and 800 °C, respectively. The geometry of these specimens is shown in Fig. 9(a), and the first batch of damaged specimens after the experiments is shown in Fig. 9(b). The averaged true stress–strain curves obtained from these experiments are shown in Fig. 10. The results demonstrated an increase in failure strain and a reduction in the ultimate strength of the material with the increase in temperature. The change in these responses is quite significant when the temperature increases from 400 to 600 °C. At 800 °C, the material behaved plastically with a constant ultimate strength of less than 40 MPa and failed with less plastic displacement than specimens at 600 °C.

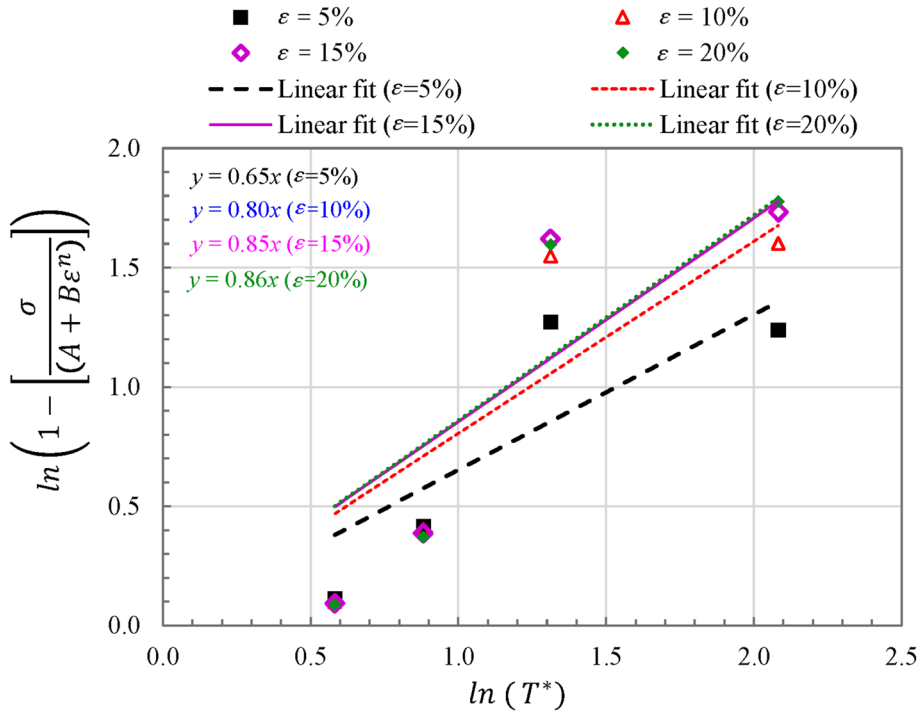

Fig. 13 Determination of m

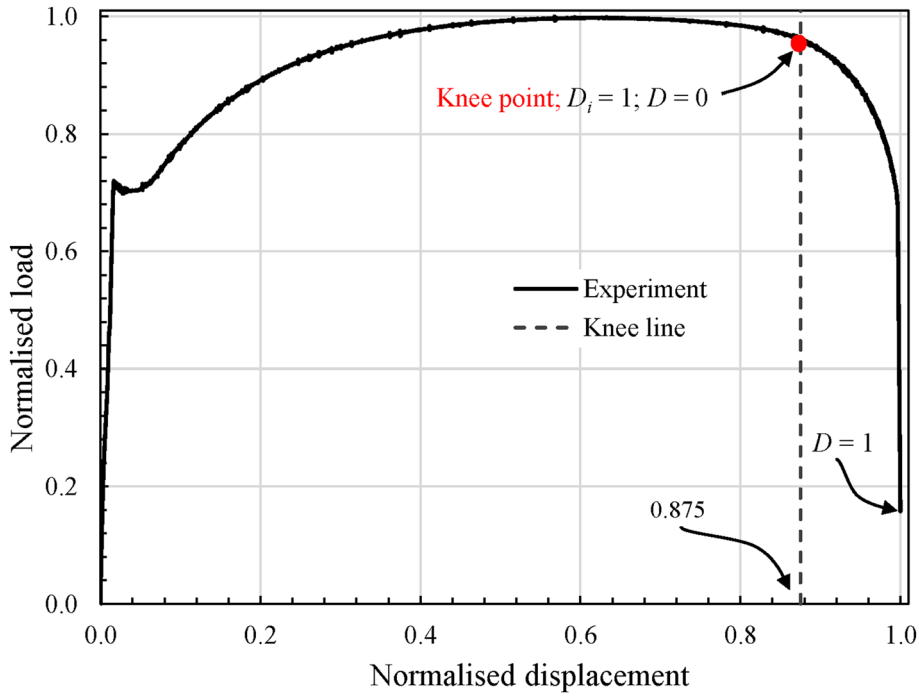

Fig. 14 Computation of accumulated critical plastic strain

4. Determination of J–C Strength and Damage Model Parameters

Johnson–Cook's five strength model parameters (*A, B, n, C,* and *m*) and five damage model parameters (D_1 to D_5) are extracted from sixteen different types of experiments discussed in Section 3.

4.1 J–C Strength Model Parameters

4.1.1 Determination of A, B, n. The parameters *A, B,* and *n* in Eq 1 are determined from the tensile experiments conducted at a strain rate, $\dot{\varepsilon} = 0.0003\ s^{-1}$ and room temperature $T = 30$ °C. Parameter *A* is the initial yield strength and is found as 252.3 MPa from the experiment. For determining the strain hardening coefficient *B* and strain hardening exponent *n*, stress–strain data in the strain hardening region up to the maximum strength are used. The data from the experiment are considered to be at a reference strain rate, i.e. $\dot{\varepsilon}_0 = 0.0003\ s^{-1}$, and the reference temperature is taken as $T_0 = 30$ °C which is also considered as the room temperature *T*. This, in turn, will lead to $\dot{\varepsilon}^* = \dot{\varepsilon}/\dot{\varepsilon}_0 = 1$ and $T^* = 0$. Substituting these values in Eq 1 yields the second and third terms as 1 and results in the following expression:

$$(\sigma - A) = B(\varepsilon)^n \qquad \text{(Eq 12)}$$

The strain hardening region from the stress–strain data is plotted as $(\sigma - A)$ against ε as shown in Fig. 11. A trend line with power fit to this data gives the values matching the form in Eq 12 where $B = 466.72$ MPa and $n = 0.5447$.

4.1.2 Determination of C. Data from experiments conducted at eight different strain rates (as given in Table 2) at room temperature $T = 30$ °C, which is also considered as reference temperature T_0, are used for determining *C*. This will lead to $T^* = 0$. Substituting this value in Eq 1 yields the third term as 1, and the equation can be written as follows:

$$\frac{\sigma}{(A + B\varepsilon^n)} - 1 = C \ln(\dot{\varepsilon}^*) \qquad \text{(Eq 13)}$$

Using Eq 13, eight data points can be obtained for the left-hand side (LHS) term at any given plastic strain (say 5 or 10%) from stress–strain curves. Considering $\dot{\varepsilon}_0 = 0.0003\ s^{-1}$, eight different strain rates $\dot{\varepsilon}$ give eight corresponding data points for the right-hand side (RHS) term of Eq 13. Plot of eight LHS data points against corresponding RHS data for 5 and 10% plastic strain is shown in Fig. 12.

Linear fit of these eight data points at 5 and 10% plastic strains gives a value of *C* as 0.0511. However, a significant difference is observed between the actual data points with respect to the linear fit. In order to minimise this error, *C* is calculated between a given range of strain rates as 0.010 for $\dot{\varepsilon} < 0.3\ s^{-1}$; 0.016 for $0.3\ s^{-1} \geq \dot{\varepsilon} \leq 1\ s^{-1}$; and 0.0511 for $\dot{\varepsilon} > 1\ s^{-1}$.

4.1.3 Determination of m. In the present work, isothermal heating is considered, and load induced adiabatic heating is neglected to retain the simplistic nature of the original J–C work. Thermal softening exponent *m* in Eq 1 can be determined from the results of tensile experiments conducted at four different elevated temperatures, as mentioned in Table 2, and

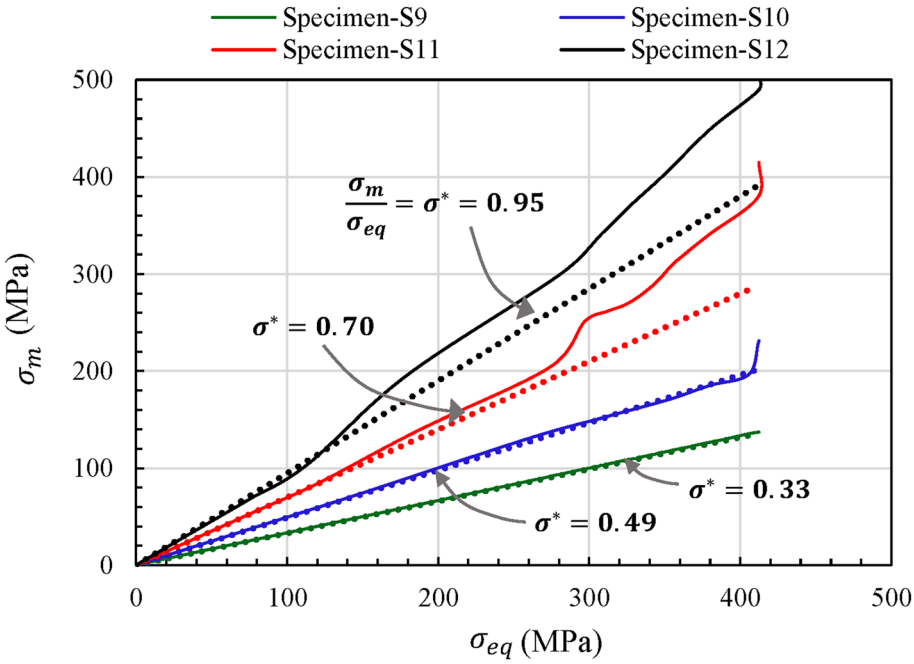

Fig. 15 Obtaining stress triaxiality of notched specimens (9–12 shown in Fig. 7)

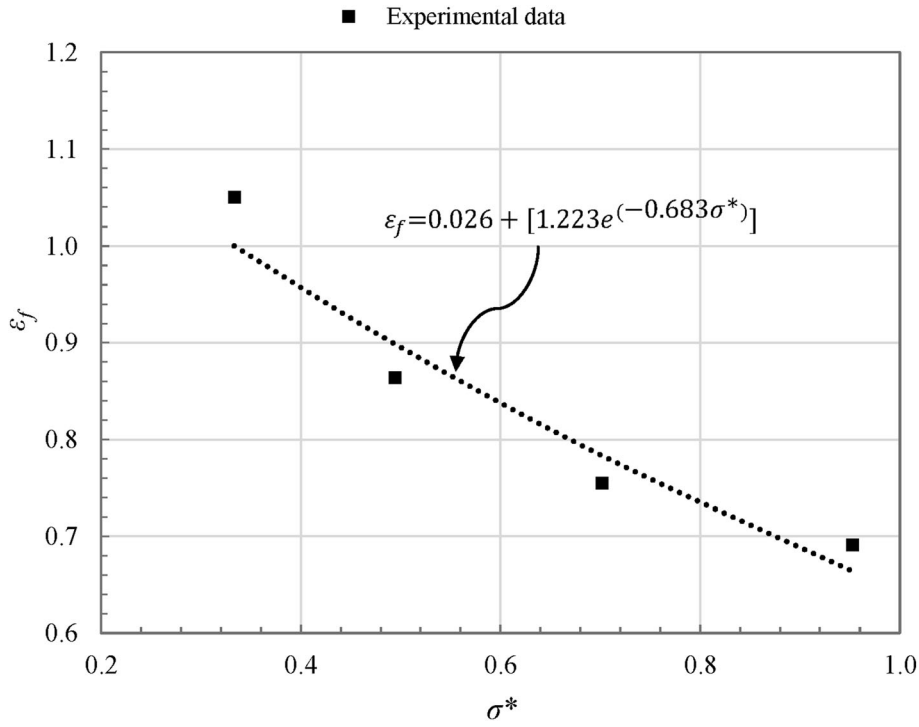

Fig. 16 Determination of D_1, D_2 and D_3

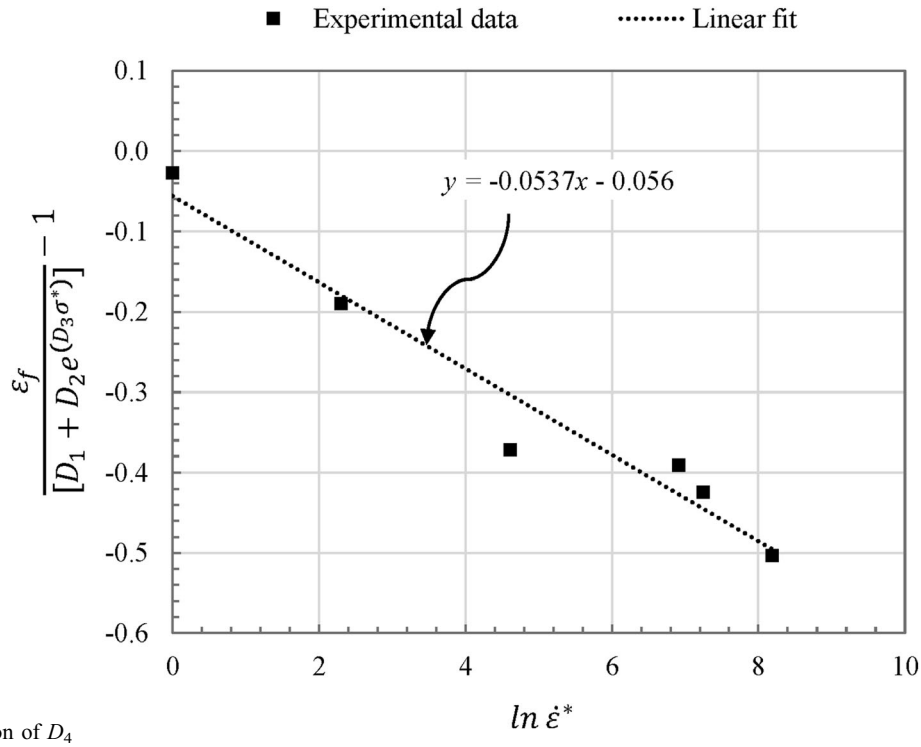

Fig. 17 Determination of D_4

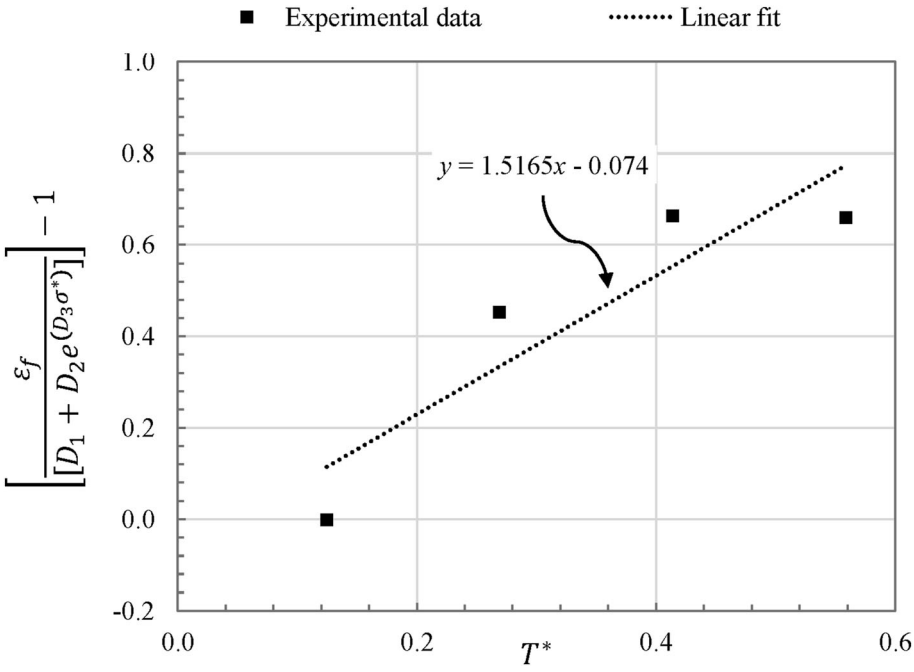

Fig. 18 Determination of D_5

Table 3 Determined parameters of Johnson–Cook strength and damage models

J–C strength model	A (MPa)	B (MPa)	n	C	m
	252.3	466.7	0.545	0.010 ($\dot{\varepsilon} < 0.3s^{-1}$) 0.016 ($0.3s^{-1} > \dot{\varepsilon} < 1s^{-1}$) 0.051 ($\dot{\varepsilon} > 1s^{-1}$)	0.79
J–C damage model	D_1	D_2	D_3	D_4	D_5
	0.026	1.223	− 0.683	− 0.054	1.517

their stress–strain behaviours are shown in Fig. 10. The reference temperature is T_0 = 30 °C, and the melting temperature is T_m = 1415 °C. These experiments were conducted at a strain rate, $\dot{\varepsilon} = 0.0003\ s^{-1}$, and as earlier, considering the reference strain rate as $\dot{\varepsilon_0} = 0.0003\ s^{-1}$, the second term in Eq 1 leads to unity. The Eq 1 can now be written as follows:

$$\ln\left(1 - \frac{\sigma}{(A + B\varepsilon^n)}\right) = m \ln(T^*) \quad \text{(Eq 14)}$$

Using Eq 14, four data points for LHS and RHS terms can be obtained at four different temperatures at plastic strains of 5, 10, 15, and 20%. The LHS term is plotted against the RHS term at four different temperatures for the considered plastic strains, as shown in Fig. 13. The linear trend line fits between these data points at each value of plastic strain gives the value of m as the slope of these lines. The slopes at four values of plastic strains, i.e. 5, 10, 15, and 20%, respectively, resulted in values of m as 0.6515, 0.805, 0.8537, and 0.8597. The average value of m is found to be 0.79.

4.2 J–C Damage Model Parameters

Five different J–C's damage model parameters D_1–D_5 are determined from the results of different tensile experiments. The procedures are detailed in this section.

4.2.1 Failure Strain from Experiments. Failure strain is given by the expression (Ref 3, 13):

$$\varepsilon_f = \ln\left(\frac{A_0}{A_f}\right) \quad \text{(Eq 15)}$$

where A_0 is the initial cross-sectional area of the specimen at gauge length location before the experiment, and A_f is the cross-sectional area after the experiment. The failure strain in each experiment is obtained by measuring the cross-sectional area of the specimens before and after the experiments and from Eq 15.

From the average normalised load-deflection curve of the plain specimens at reference strain rate and temperatures shown in Fig. 14, it can be observed that, at a certain point of deflection, load gradually reduces when deflection reaches a critical value. After reaching the critical value, a sudden reduction in load can be observed. This location is assumed to

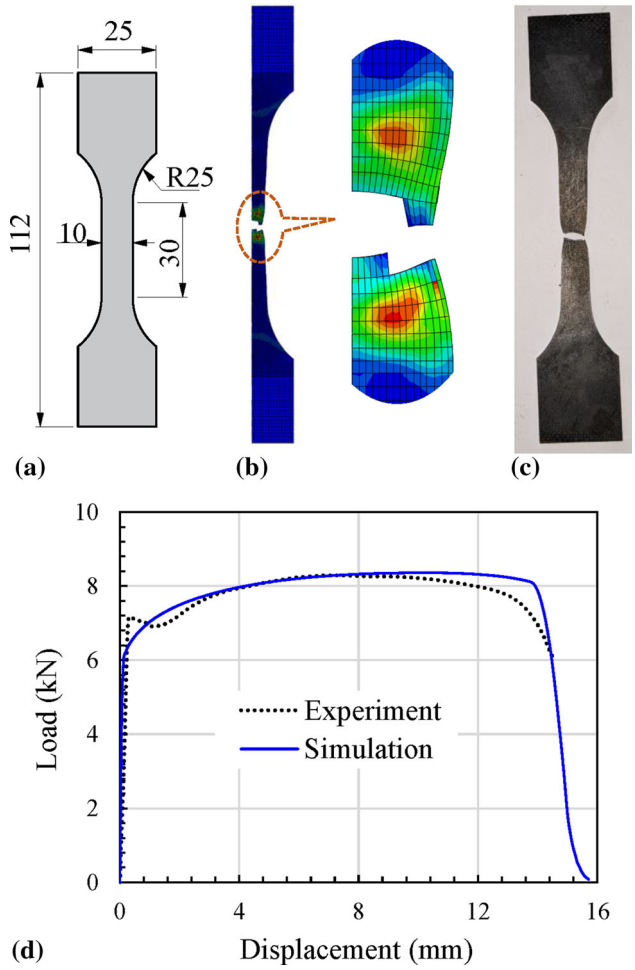

Fig. 19 Comparison of experimental and J–C model predictions for plain tensile specimen. (a) Specimen Geometry (all dimensions in mm). (b) FEA model. (c) Experimented Specimen. (d) Experimental vs. predicted results

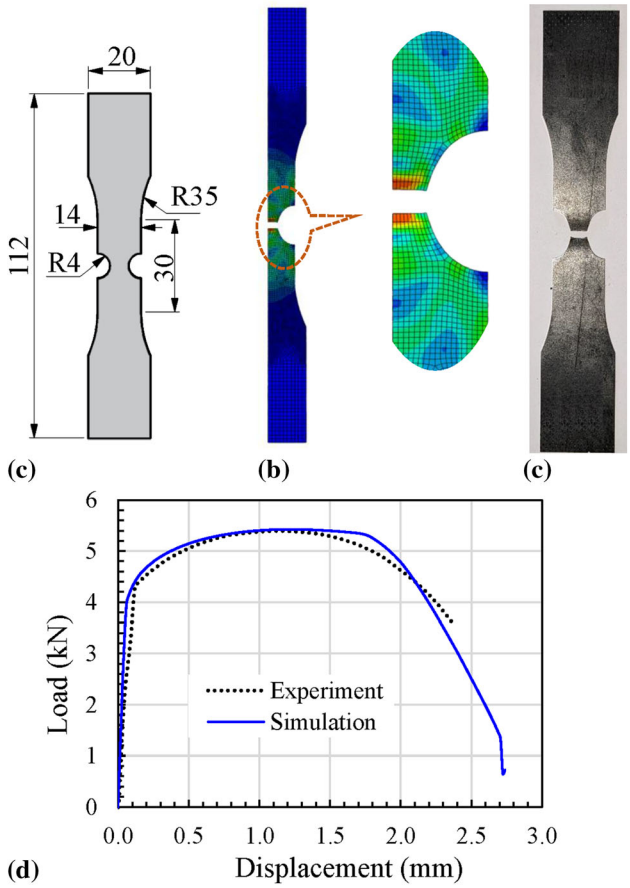

Fig. 20 Comparison of experimental and J–C model predictions for a notched tensile specimen. (a) Specimen geometry (all dimensions in mm). (b) FEA model. (c) Experimented specimen. (d) Experimental vs. predicted results

be the point of change in curvature for the load-displacement curve between maximum load and failure. This location of the change in curvature (knee point) is found using the Kneedle algorithm proposed in Ref 14. This value is 87.5% of the total deflection. The critical value of accumulated plastic strain is also assumed to be equal to 87.5% of the fracture strain. In the present work, all the J–C failure parameters are computed by considering the critical value of plastic strains instead of fracture strains.

4.2.2 Determination of Stress Triaxiality of Notched Specimens. FEA simulations are conducted on the notched specimens shown in Fig. 7(a) using the J–C constitutive parameters obtained in Sect. 4.1. Curves obtained by plotting mean stress to von-Mises stress in the centre element at the middle cross section of the specimens are shown in Fig. 15. The slope of these curves remains almost constant within the elastic stage and continuously increases in the plastic stage. In the present work, the stress triaxiality of each specimen is obtained by plotting the linear curve fit to this data within the elastic limit where the distortion of the element is negligible. The values of stress triaxialities are found to be 0.33, 0.49, 0.7, and 0.95 for the specimens S9, S10, S11, and S12, respectively.

4.2.3 *Determination of D_1, D_2, and D_3.* The values of damage model parameters D_1, D_2, and D_3 are determined from tensile experiments of notched specimens conducted at a strain rate $\dot{\varepsilon} = 0.0003\ s^{-1}$ and at temperature $T = 30\ °C$. Considering the reference strain rate as $\dot{\varepsilon}_0 = 0.0003\ s^{-1}$ and reference temperature as $T_0 = 30\ °C$, will lead to $\dot{\varepsilon}^* = \dot{\varepsilon}/\dot{\varepsilon}_0 = 1$ and $T^* = 0$. Substituting these values in Eq 3 yields the second and third terms as 1 and results in the following expression:

$$\varepsilon_f = D_1 + D_2 e^{(D_3 \sigma^*)} \qquad \text{(Eq 16)}$$

The data of experimental failure strain ε_f are plotted against the respective stress triaxiality σ^* in Fig. 16. Fitting the curve based on Eq 16 to these data points by adopting minimisation of errors based on least squares gives values for D_1, D_2, and D_3 as 0.026, 1.223, and − 0.683, respectively.

4.2.4 *Determination of D_4.* The value of D_4 can be determined from the results of tensile experiments conducted at six different strain rates at temperature $T = 30\ °C$, as given in Table 2. Considering the reference temperature as $T_0 = 30\ °C$ leads to $T^* = 0$, which in turn results in the third term in Eq 3 attaining a value of 1, and the equation reduces to:

$$\frac{\varepsilon_f}{[D_1 + D_2 e^{(D_3 \sigma^*)}]} - 1 = D_4 \ln \dot{\varepsilon}^* \qquad \text{(Eq 17)}$$

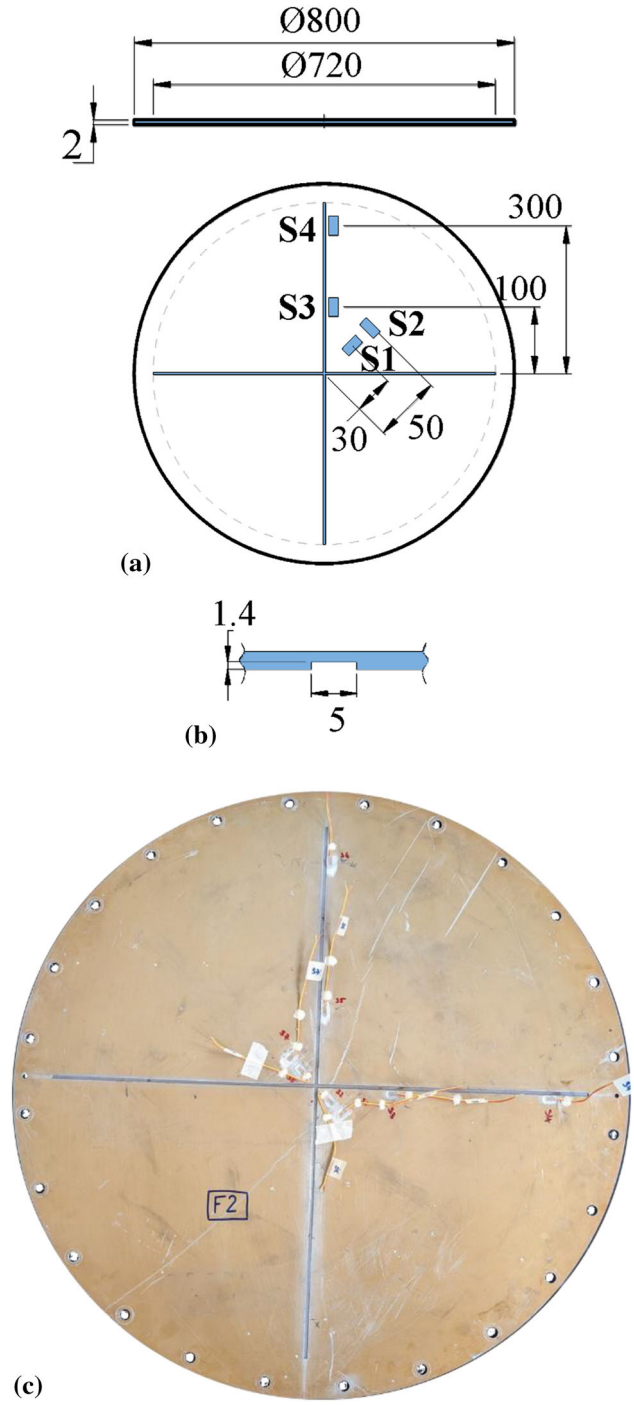

Fig. 21 Experimental burst disc geometry (all dimensions in mm). (a) Geometry of flat burst disc. (b) Score geometry. (c) Flat burst disc

Reference strain rate is considered as $\dot{\varepsilon}_0 = 0.0003\ \mathrm{s}^{-1}$. Using Eq 17, six data points are obtained for the LHS term from stress–strain curves. The plot of these six LHS data against corresponding RHS data is shown in Fig. 17. A linear trend line fit to the data points provides its slope as $D_4 = -0.0537$.

4.2.5 ***Determination of D_5.*** The value of D_5 is determined from the results of tensile experiments conducted at four different elevated temperatures. Since all these experiments were conducted at the reference strain rate of $0.0003\ \mathrm{s}^{-1}$ itself, the second term in Eq 3 leads to unity, and the equation can be written as follows:

$$\frac{\varepsilon_f}{[D_1 + D_2 e^{(D_3\sigma^*)}]} - 1 = D_5 T^* \qquad \text{(Eq 18)}$$

Using Eq 18, four data points for LHS and RHS terms can be obtained at four different temperatures and are plotted as shown in Fig. 18. The linear trend line fit between these data points gives the value of slope as $D_5 = 1.517$.

4.3 Damage Evolution

In the present work, a different approach is followed to implement damage initiation and evolution to use the default input parameters available in Abaqus Explicit (Ref 15). As explained in sect. 2.2 and 4.2.1, the damage initiates when the accumulated plastic strain in the material reaches the critical value of plastic strain given by Eq 2 and is shown in Fig. 1. All the J–C damage parameters thus computed will define this critical plastic strain at which damage initiates. Then, the damage evolution is implemented in Abaqus (Ref 15) using the fracture mechanic-based stress–displacement response proposed by Hillerborg et al. (Ref 16) instead of the stress–strain response in order to reduce mesh dependency due to strain localisation. Stress in the material element in a damaged state, σ_D in this phase is defined by Eq 4, and the value of D is obtained by assuming a linear relationship between u^{pl}, the effective plastic displacement and damage variable which is given by:

$$D = \frac{u^{\mathrm{pl}}}{u_f^{\mathrm{pl}}} \qquad \text{(Eq 19)}$$

where u_f^{pl} is the plastic displacement at failure. Hillerborg et al. (Ref 16) proposed that the crack is assumed to propagate when stress at the crack tip reaches the tensile strength of the material, σ_y and the amount of fracture energy G_f, absorbed per widening the unit crack area is given by:

$$G_f = \int_0^{w_l} \sigma_y \mathrm{d}w \qquad \text{(Eq 20)}$$

where w_l is the crack tip opening displacement equivalent to u_f^{pl}.

It is implemented in Abaqus (Ref 15) as follows:

$$G_f = \frac{\sigma_y u_f^{\mathrm{pl}}}{2} \qquad \text{(Eq 21)}$$

G_f is a material parameter and can be represented by the area under the stress–displacement curve of the pre-notched specimen. In the present work, the area under the load-displacement curve of the notched specimen (i.e. Specimen-11(a and b) shown in Fig. 7(a)) per unit cross-sectional area is taken as the fracture energy required for opening unit area of the crack, which is found to be 224.6 N/mm.

The element will be deleted when $D = 1$, i.e. when plastic displacement in the material reaches plastic displacement at failure obtained from Eq 21, which is implemented as a default algorithm in Abaqus explicit FEA code (Ref 15).

The summary of determined values of J–C's five strength model parameters and five damage model parameters is provided in Table 3.

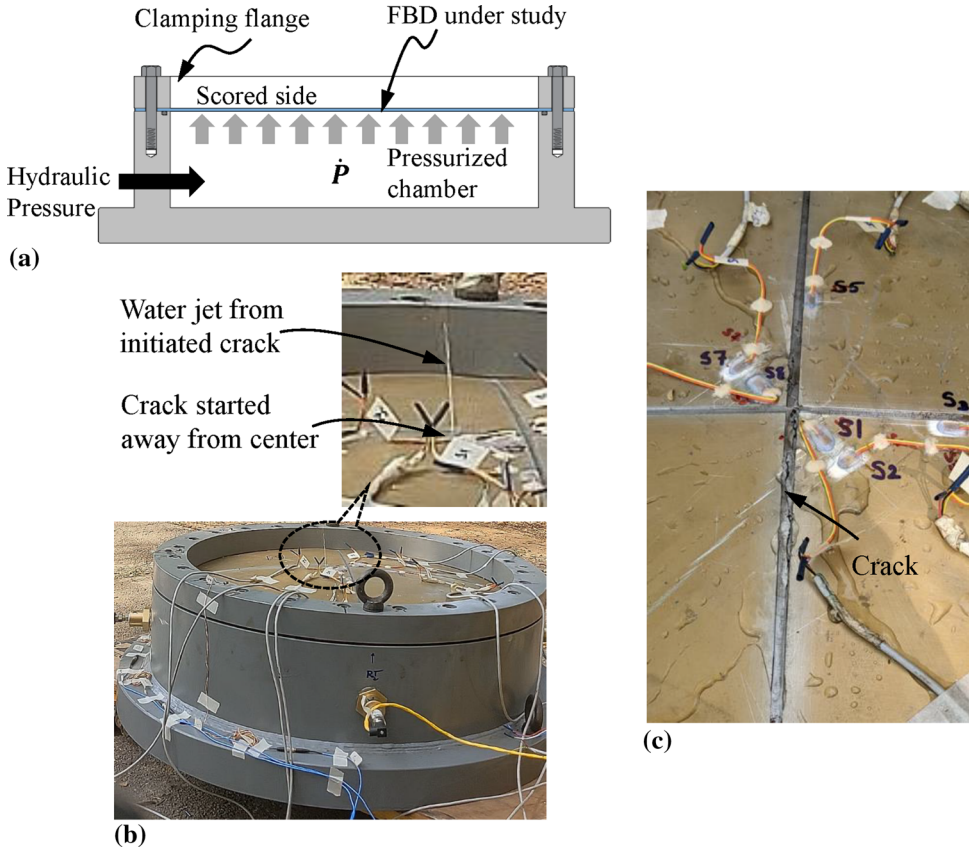

Fig. 22 Hydrostatic experiment of the flat burst disc. (a) Schematic view of the experimental setup. (b) Flat burst disc at the instant of failure. (c) Propagated crack

5. Experimental Validation of Determined J–C Model Parameters

To validate the determined J–C's strength and damage model parameters, three experimental data are compared with respect to FEA simulation results. The first one is the average load-displacement curve of tensile experiments conducted at 1.08 s^{-1} strain rate, the second one is the load-displacement curve of a separate notched specimen tensile tested at 0.3 s^{-1} strain rate, and the third one is a comparison of pressure-strain curves from the burst experiment of a flat burst disc. The experiments are numerically simulated in Abaqus Explicit (Ref 15) using the determined model parameters and damage evolution approach thus discussed.

5.1 Validation-1: Plain Tensile Specimen

The tensile experiment of plain specimen at 1.08 s^{-1} strain rate is considered to validate the determined J–C model parameters. Specimen geometry and the fractured specimens are shown in Fig. 19(a) and (c). The half model is discretised using 19610 C3D8R eight-node solid brick elements with reduced integration and a symmetric boundary condition is adopted. A maximum element size of 0.5 mm is retained. The FEA model is fixed at one end, a displacement loading of 65 mm/s is applied at the other end, and the simulation is continued until the failure of the specimen, where the failed specimen is shown in Fig. 19(b). The specimen failed at the minimum cross-sectional region in the middle. A good agreement is obtained on the failed pattern between the experiment and simulation. Further, the load-displacement curves obtained from experiment and simulation are shown in Fig. 19(d). The results are in close agreement with each other. Thus, the predicted load-displacement response and failure pattern matched closely with experimental results.

5.2 Validation-2: Notched Tensile Specimen

In the second independent validation, a notched specimen prepared with a stress triaxiality of 0.49 is subjected to a tensile experiment at a strain rate of 0.3 s^{-1}. Specimen geometry and the fractured specimens are shown in Fig. 20(a) and (c). The half model is discretised using 19490 C3D8R eight-node solid brick elements with reduced integration, and a symmetric boundary condition is applied. A maximum element size of 0.5 mm is adopted from a mesh convergence study. The FEA model is fixed at one end, a displacement loading of 10 mm/s is applied at the other end, and the simulation is allowed to run until the failure of the specimen. The failed specimen in the simulation is shown in Fig. 20(b). The specimen failed at the minimum cross-sectional region in the notched region. A good

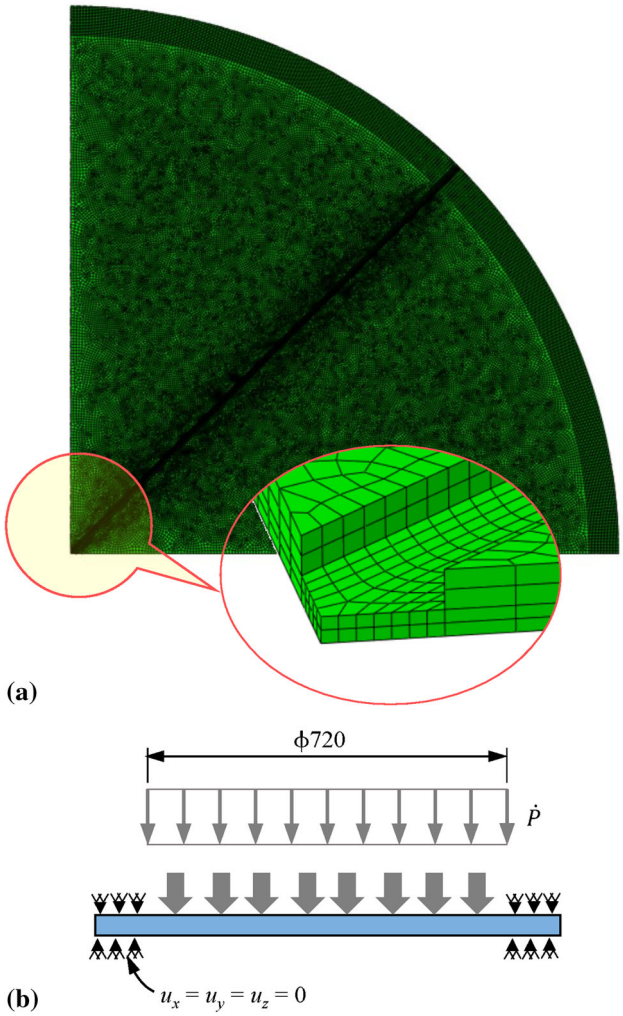

Fig. 23 FEA simulation setup for the flat burst disc. (a) FE model. (b) Loads and boundary conditions

agreement is obtained on the failed pattern between the experiment and simulation. Further, the load-displacement curves obtained from experiment and simulation are shown in Fig. 20(d). The results are in close agreement with each other. Both the load-displacement response and failure pattern from the simulation matched closely with experimental results, thereby validating the accuracy of the determined model parameters.

5.3 Validation-3: Hydrostatic Burst Experiment of Flat Burst Disc (FBD)

In addition to the previous two independent validations on plain and notched tensile specimens, the third validation is carried out by conducting an elaborate experiment on a flat burst disc (FBD) subjected to hydraulic pressure until failure and comparing the strains developed within the disc at four locations with that obtained from FEA simulation.

5.3.1 Geometry of FBD and Experiment. The geometry of the FBD used is shown in Fig. 21(a). It is a circular disc of 800 mm diameter laser cut from a 2 mm thick hot rolled sheet of the same material. Two rectangular scores with a width of 5 mm and a depth of 1.4 mm are milled in a ' + ' configuration, as shown in Fig. 21(b). The FBD used in the experiment is shown in Fig. 21(c).

A schematic view of the burst experimental setup of the FBD is shown in Fig. 22(a). The disc is clamped at the end of a pressurised cylindrical chamber with the opening diameter of 720 mm (diameter of the disc on which fluid pressure is applied). A quartz-based pressure transducer with an accuracy of 2% and a response time of 0.5 ms is attached to the chamber to record the pressure inside the chamber during the test. Four foil-type strain gauges, S1, S2, S3, and S4, having a nominal resistance of 350Ω, are bonded to the scored side of the FBD, as shown in Fig. 21(a), to record the strain response of the disc under applied pressure. Two strain gauges, S1 and S2, are placed at 45^0 to the score and closer to the centre of the disc, one in radial and another in the tangential direction, at a distance of 50 mm and 30 mm, respectively. Two other strain gauges, S3 and S4, are placed on the disc, aligned to the groove, one nearer the centre at 100 mm and another nearer to the clamping end of the disc at 300 mm from the disc centre.

The actual experimental setup is shown in Fig. 22(b). Before the experiment, the chamber is pre-filled with water, and additional hydraulic pressure is applied during the experiment at a quasi-static loading rate of 0.0003 MPa/s until the burst pressure P_b of the disc is reached. The observed P_b is 0.331 MPa which took about 992 seconds to form the initial crack. It is observed that the fracture is initiated away from the centre of the disc, as shown in the inset of Fig. 22(c) and propagated along one score until the pressure drops due to water leakage. Strain response at four locations under applied pressure is continuously monitored until the chamber pressure drops to zero.

5.3.2 FEA Simulation of FBD. The Abaqus/Explicit is adopted for creating the numerical model of the FBD, as shown in Fig. 23(a) and its FEA simulation. The quarter model is modelled in 3D, and symmetric boundary conditions are applied. Automatic time increment is employed. The model is discretised with 246558 numbers of C3D8R element, an eight-node brick element with reduced integration and hourglass control. All three displacement degrees of freedom of nodes in the annular area of the disc between diameters 720 and 800 mm (see Fig. 21(a)) are fully constrained, as shown in Fig. 23(b). A uniformly distributed pressure load is applied on the plain side of the disc. In order to simulate the problem in nonlinear explicit FEA with economic computation, the loading rate is accelerated based on the approach provided by Baker et al. (Ref 17) for the shock response of a blast-loaded elastic oscillator to calculate the loading rate for the simulation, wherein for a quasi-static loading regime, the ratio of loading duration t_d with respect to the natural time period $(1/\omega_n)$ is given as follows:

$$\omega_n t_d \geq 40 \qquad \text{(Eq 22)}$$

From the modal analysis of the FBD shown in Fig. 23(a), the fundamental natural frequency ω_n is found to be 36.67 Hz. From Eq 22, t_d is computed as 1.09 s. Considering the

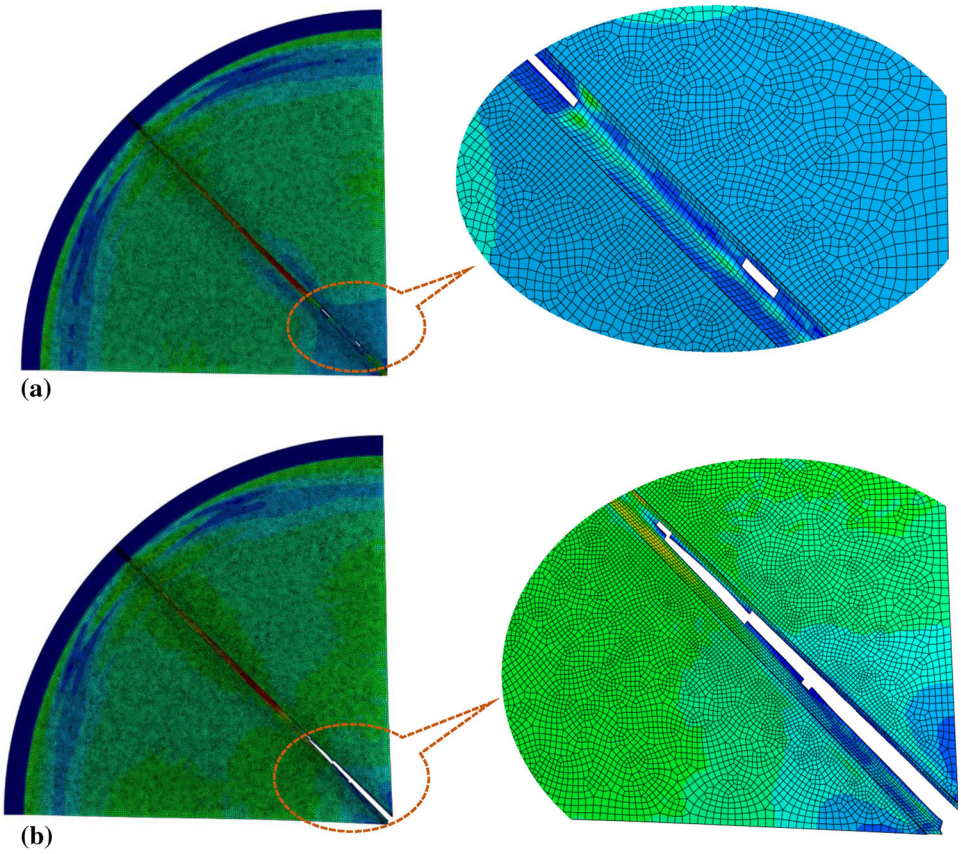

Fig. 24 FEA simulation results. (a) Initiation of the crack in the score region (P = 0.327 MPa). (b) Propagation of crack in the score region

experimentally achieved P_b of 0.331 MPa and the calculated t_d, the rate of loading for simulation is taken as 0.3 MPa/s. A mesh convergence study is carried out to find the optimum number of elements through the thickness of the FBD, and the model with 4 elements through the plate thickness, i.e. 0.5 mm of element size, gave an economical and converged solution, which is considered for comparison and validation of FEA simulation with experimental results.

5.3.3 Comparison Between FEA Simulation and Burst Experiment. At this loading rate of 0.3 MPa/s, it is observed from the simulation that the strain is concentrated along the score at the central region of the disc. The failure is initiated at the score location away from the centre of the disc, as seen in Fig. 24(a). This failure is initiated when the accumulated plastic strain reaches the fracture strain. Subsequently, failure propagated towards the centre of the disc upon further loading, as observed in Fig. 24(b). A similar behaviour is observed during the experiment, as shown in Fig. 22(b) and (c). The simulation using the determined J–C's material and damage model parameters resulted in the burst pressure of 0.327 MPa as against 0.331 MPa recorded in the experiment. The normal strain in the direction of the uniaxial strain gauge predicted from the FEA simulation is compared with the experimentally observed strain values at the four strain gauge locations S1, S2, S3, and S4, as shown in Fig. 25. The predicted strain profiles matched very closely with that of the experiment. Thus, close agreements are found between the simulation and experiment on the failure pattern up to initiation of the burst, burst pressure, and strain profiles, thereby validating the determined material and damage parameters of J–C model.

6. Conclusions

Johnson–Cook strength and damage models are very popular in numerically simulating the large deformation, strain and strain rate hardening, thermal softening, and damage initiation in ductile materials undergoing loadings at low to high strain rates. This paper has presented the experimental determination of ten different Johnson–Cook's strength and damage model parameters for E250 structural steel. The parameters have been determined from the results of sixteen types of experiments conducted at various strain rates (0.0003–8000 s^{-1}), stress triaxialities (0.33–0.95), and temperatures (30–800 °C). Three values of the strain hardening coefficient are proposed for various ranges of strain rates. Determined J–C's strength and damage model parameters have been employed in numerically simulating the experiments of a separate i) plain tensile specimen, ii) a notched tensile specimen, and iii) burst disc under hydrostatic loading. The stress–strain response of plain and notched tensile specimens, the pressure-strain response of the flat burst disc, and the failure

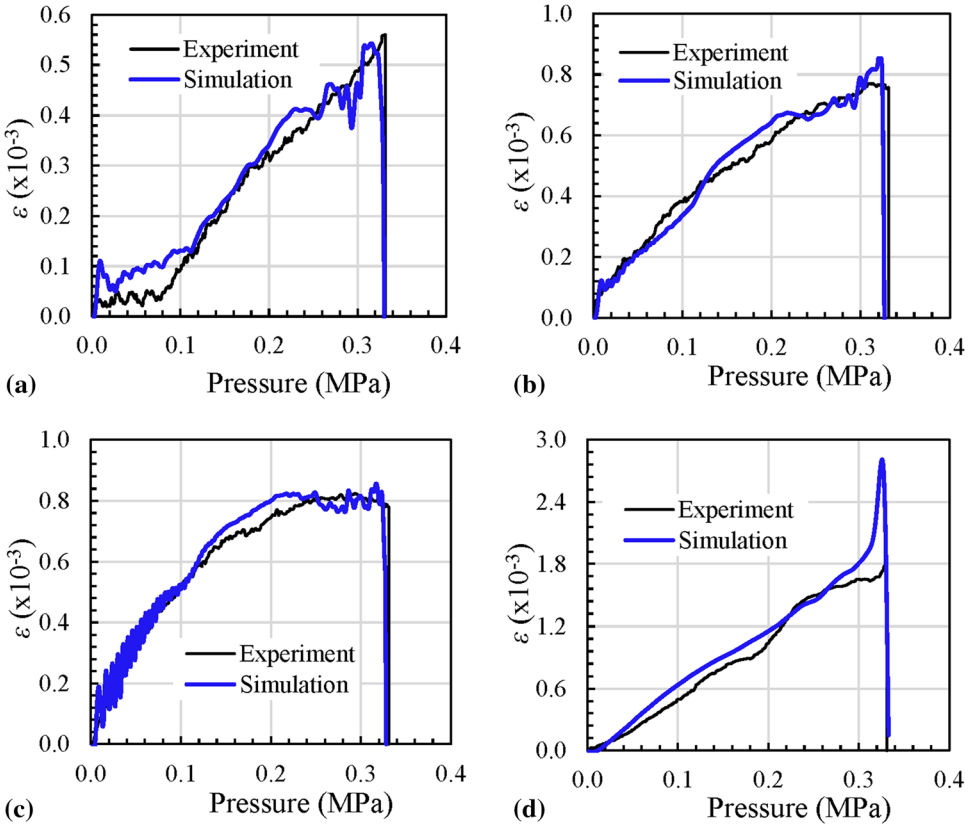

Fig. 25 Comparison of normal strains between simulations based on determined J–C model parameters and experiments at locations mentioned in Fig. 21(a). (a) Location-1 at S1 (45° from horizontal-left score). (b) Location-2 at S2 (135° from horizontal-left score). (c) Location-3 at S3 (along score near to centre). (d) Location-4 at S4 (along score near to fixity)

pattern from all three simulations, including the burst pressure in the third simulation, agreed, respectively, with the three experiments, thereby validating the determined J–C's strength and damage model parameters. The methodology has been explained step-by-step, which can be followed for determining the J–C model parameters of any ductile material. The determined model parameters can be directly used in any commercially available nonlinear explicit FEA codes.

Acknowledgments

The authors thank the support provided by Mr. Swati Kiran, Research Scholar at IIT Hyderabad and engineers at our Laboratory in conducting various experiments.

Data Availability

All the data required to reproduce these findings are provided in the manuscript as graphs instead of raw data. This is also used as part of an ongoing study by the authors.

Conflict of interest

On behalf of all authors, the corresponding author states that there is no conflict of interest. The authors have no competing interests to declare that are relevant to the content of this article.

References

1. C.L. Rao, V. Narayanamurthy, and K.R.Y. Simha, *Applied Impact Mechanics*, Wiley, Hoboken, 2016. https://doi.org/10.1002/9781119241829
2. G.R. Johnson and W.H. Cook, A Constitutive Model and Data from Metals Subjected to Large Strains, High Strain Rates and High Temperatures. In: Proceedings: Seventh International Symposium on Ballistics, Netherlands. 541–547 (1983)
3. G.R. Johnson and W.H. Cook, Fracture Characteristics of Three Metals Subjected to Various Strains, Strain Rates, Temperatures and Pressures, *Eng. Fract. Mech.*, 1985, **21**(1), p 31–48. https://doi.org/10.1016/0013-7944(85)90052-9
4. K. Vedantam, D. Bajaj, N.S. Brar, and S. Hill, Johnson - Cook Strength Models for Mild and DP 590 Steels, *AIP Conf. Proc.*, 2006, **845**(1), p 775–778. https://doi.org/10.1063/1.2263437
5. Z. Xu and F. Huang, Plastic Behavior and Constitutive Modelling of Armor Steel Over Wide Temperature and Strain Rate Ranges, *Acta Mech. Solida Sin.*, 2012, **25**(6), p 598–608. https://doi.org/10.1016/S0894-9166(12)60055-X
6. A. Banerjee, S. Dhar, S. Acharyya, D. Datta, and N. Nayak, Determination of Johnson Cook Material and Failure Model Constants and Numerical Modelling of Charpy Impact Test Of Armour Steel, *Mat. Sci. Eng. A*, 2015, **640**, p 200–209. https://doi.org/10.1016/j.msea.2015.05.073
7. H.K. Farahani, M. Ketabchi, and S. Zangeneh, Determination of Johnson–Cook Plasticity Model Parameters for Inconel 718, *J. Mat. Eng. Perform.*, 2017, **26**(11), p 5284–5293. https://doi.org/10.1007/s11665-017-2990-2
8. M. Murugesan and D.W. Jung, Johnson Cook Material and Failure Model Parameters Estimation of AISI-1045 Medium Carbon Steel for Metal Forming Applications, *Materials.*, 2019, **12**(4), p 609. https://doi.org/10.3390/ma12040609

9. G.H. Majzoobi and F.R. Dehgolan, Determination of the Constants of Damage Models, *Proced. Eng.*, 2011, **10**, p 764–773. https://doi.org/10.1016/j.proeng.2011.04.127
10. B. Bal, K.K. Karaveli, B. Cetin, and B. Gumus, The Precise Determination of the Johnson–Cook Material and Damage Model Parameters and Mechanical Properties of an Aluminum 7068–T651 Alloy, *J. Eng. Mat. Tech.*, 2019, **141**(4), p 141001. https://doi.org/10.1115/1.4042870
11. T. Børvik, M. Langseth, O.S. Hopperstad, and K.A. Malo, Ballistic Penetration of Steel Plates, *Int. J. Imp. Engg.*, 1999, **22**(9–10), p 855–886. https://doi.org/10.1016/S0734-743X(99)00011-1
12. J. Lemaitre, *A Course on Damage Mechanics*, Springer, Berlin Heidelberg, 2012
13. R.W. Hertzberg, *Deformation and Fracture Mechanics of Engineering Materials*, Wiley, United Kingdom, 1996
14. V. Satopaa, J. Albrecht, D. Irwin, and B. Raghavan, Finding a "Kneedle" in a Haystack: Detecting Knee Points in System Behavior. In: 31st International Conference on Distributed Computing Systems Workshops. 166-171 (2011) doi: https://doi.org/10.1109/ICDCSW.2011.20
15. Abaqus User Manual, V6.14: Dassault Systèmes Simulia Corporation, France (2014)
16. A. Hillerborg, M. Modéer, and P.E. Petersson, Analysis of Crack Formation and Crack Growth in Concrete by Means of Fracture Mechanics and Finite Elements, *Cem. Concr. Res.*, 1976, **6**(6), p 773–781. https://doi.org/10.1016/0008-8846(76)90007-7
17. W.E. Baker, P.A. Cox, J.J. Kulesz, R.A. Strehlow, and P.S. Westine, *Explosion Hazards and Evaluation*, Elsevier Science, Netherlands, 2012